



The Environment and Star Formation around the Infrared Bubble N 13

Dong-Dong Zhou¹, Jian-Jun Zhou^{1,2,3}, Gang Wu^{1,4}, Jarken Esimbek^{1,2,3}, and Ye Xu⁵

¹Xinjiang Astronomical Observatory, Chinese Academy of Sciences, Urumqi 830011, China; zhoudongd@xao.ac.cn

²Key Laboratory of Radio Astronomy, Chinese Academy of Sciences, Urumqi 830011, China

³Xinjiang Key Laboratory of Radio Astrophysics, Urumqi 830011, China

⁴Max-Planck-Institut für Radioastronomie, Auf dem Hügel 69, D-53121 Bonn, Germany

⁵Purple Mountain Observatory, Chinese Academy of Sciences, Nanjing 210033, China

Received 2022 May 22; revised 2022 October 29; accepted 2022 November 7; published 2022 December 14

Abstract

Infrared bubbles provide a unique opportunity to study the interactions between massive stars and surrounding material. We conduct a multi-wavelength study on the environment and star formation around an infrared bubble N 13. Three dust clumps and two molecular clumps are identified around N 13, which are all distributed on the layer. Young stellar objects (YSOs) are carefully searched using infrared colors and YSO candidates of WISE and Gaia DR2, and three Class I/II YSOs are found in N 13. In addition, four O-type stars identified in N 13 are probably the exciting stars. The dynamical and fragmentation ages of N 13 are 0.32–0.35 and 1.37–2.80 Myr respectively, which suggest that the radiation-driven implosion model may be dominant in N 13. By comparing the small-size bubble N 13 ($R \sim 1.9$ pc) and the larger-size bubble G15.684-0.29 ($R \sim 15.7$ pc) we found that star formation activity is more active in the large-size bubble. Brief comparisons of ten bubbles show that small-size bubbles have a small ratio of kinetic age versus the fragmentation time. Triggering star formation may be more active in bubbles with larger ratio between kinetic and fragmentation ages. Furthermore, the collect and collapse mechanism may play the dominant role in the large-size ones.

Key words: ISM: bubbles – ISM: structure – ISM: kinematics and dynamics – stars: formation

1. Introduction

Massive stars ($M \geq 8 M_{\odot}$) are believed to have significant impacts on the ambient interstellar medium through their radiative, mechanical and chemical feedback, e.g., H II regions, jets, outflows, stellar winds and supernovae (Churchwell 2002). Infrared (IR) bubbles, which are a primary manifestation of stellar feedback (Weaver & Torres-Dodgen 1997; Churchwell 2002; Deharveng et al. 2010), are omnipresent in our Galaxy (Churchwell et al. 2006, 2007; Simpson et al. 2012). The study of bubbles gives information on the interactions of recently formed stars with their environments; in particular, information on the structure and physical properties of the stellar winds that produce the bubbles and the ambient cosmic space in which they are expanding. Therefore, IR bubbles provide a unique opportunity to study the interactions between newly formed massive stars and the surrounding material (e.g., Deharveng et al. 2010; Kendrew et al. 2012; Thompson et al. 2012; Zhang & Wang 2013).

Two major mechanisms for triggering star formation around bubbles, i.e., the collect and collapse (C&C; Elmegreen & Lada 1977) and the radiation-driven implosion (RDI; Bertoldi 1989; Lefloch & Lazareff 1994) mechanisms, are under active study recently. In the C&C model, the expanding H II region collects and compresses the swept-up material into a layer

between the ionization front (IF) and the shock front (SF). This layer between the IF and SF will become denser and possibly form second-generation young stars. On the other hand, in the RDI model, the IF drives the SF into the surrounding molecular cloud, triggering the collapse of pre-existing subcritical clumps to form new stars. Both mechanisms have been suggested in observational studies. For example, the C&C process is argued to play a more important role in bubbles N 65 and N 4 (e.g., Petriella et al. 2010; Liu et al. 2016), while the RDI model could explain the observations in bubble N 22 (e.g., Ji et al. 2012).

Generally, when the expansion of the H II region is correlated with many bubbles, this process can sweep and collect the surrounding material or compress the preexisting dense clumps. These interactions can finally result in the formation of massive stars. However, at different timescales/evolution stages of the bubble, the influence of the expanding bubble on the surroundings might be changing, and the dominant mechanism(s) of triggering star formation may also be different. Therefore, we plan to conduct a statistical study of bubbles of different sizes and seek to achieve a comprehensive understanding of bubbles and their impact on the ambient interstellar medium. A study of the largest bubble G15.684–0.29 ($R \sim 15.7$ pc) in our Milky Way has been conducted by

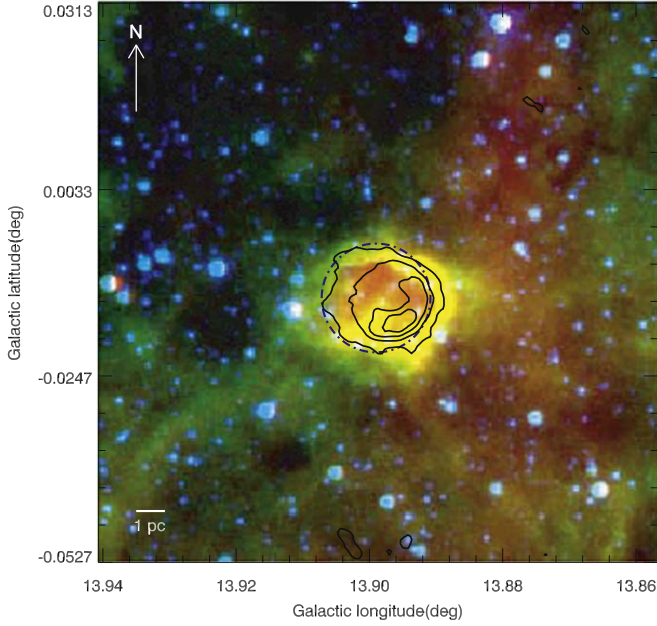


Figure 1. Composite color image of N 13 using the 3.6 (blue), 8.0 (green) and 24 μm (red) emissions. The black contours overlaid represent the MAGPIS 20 cm emission. The levels of the contours are 3, 6, 9 and $12 \times \sigma_{\text{rms}}$, where $\sigma_{\text{rms}} = 0.00065 \text{ Jy beam}^{-1}$. The blue dashed circle represents the effective radius of N 13.

Zhou et al. (2020). This paper will describe work on the small-size bubble N 13 and the results of comparing the dust clumps, molecular clumps, young stellar objects (YSOs), dynamic ages and fragmentation ages of these two bubbles.

Located at $l = 13^{\circ}900$ and $b = -0^{\circ}014$, the IR bubble N 13 enclosing H II region G013.899-00.014 (Anderson et al. 2014) was discovered by Churchwell et al. (2006). It presents a roughly ring morphology with an effective radius of about 0.49 (the blue dashed circle in Figure 1). As demonstrated in Figure 1, warm dust exists inside the cavity traced by 24 μm emission, and the thermal free-free continuum at 20 cm fills the bubble. A bright surface layer traced by 8 μm emission that surrounds N 13 presents a roughly round morphology with a small gap present in the southeast. The 20 cm and 24 μm emissions are strong in the central region of the bubble, hinting at the existence of the driven star(s) there. The 8 μm emission around the bubble suggests interactions between the H II region ionization wave front and the surrounding material.

In this work, we carry out a multi-wavelength analysis of the isolated bubble N 13. We seek to investigate the interaction of the bubble with its surroundings by studying the dense clumps around it and exploring the possible scenario to trigger star formation. This paper is organized as follows: the databases are introduced in Section 2. The results are illustrated in Section 3 and discussed in Section 4. Finally, a summary is given in Section 5.

2. Archival Data

The archival data used to analyze the IR bubble N 13 and its surroundings are derived from the Galactic Legacy Infrared Mid-Plane Survey Extraordinaire (GLIMPSE), MIPS/Spitzer Survey of the Galactic Plane (MIPSGAL), Multi-Array Galactic Plane Imaging Survey (MAGPIS), Herschel Infrared Galactic Plane Survey (Hi-GAL), CO High-Resolution Survey (COHRS), Wide-field Infrared Survey Explorer (WISE) and Two Micron All Sky Survey (2MASS).

GLIMPSE (Benjamin et al. 2003) is a mid-infrared survey (3.6, 4.5, 5.8 and 8.0 μm) of the inner Galaxy performed with the Spitzer Space Telescope. The angular resolutions are better than $2''$ at all wavelengths. The 24 μm image of N 13 is obtained from MIPSGAL (Carey et al. 2009) and the resolution at 24 μm is $6''$.

The Photoconductor Array Camera and Spectrometer (PACS; Poglitsch et al. 2010) 70 and 160 μm and the Spectral and Photometric Imaging Receiver (SPIRE; Griffin et al. 2010) 250, 350 and 500 μm IR data from Hi-GAL (Molinari et al. 2010) were used to study the dust emission around N 13. The PACS and SPIRE data sets used here are level 2.5 products produced by the Herschel Interactive Processing Environment (HIPE) software (OBSIDs: 1342218999 and 1342219000).

The $^{12}\text{CO}(3-2)$ (345.786 GHz) data, used to investigate the molecular gas, are from COHRS (Dempsey et al. 2013) acquired with the James Clerk Maxwell Telescope (JCMT) in Hawaii.

The 20 cm emission image traces the ionized gas around the bubble and is obtained from MAGPIS (White et al. 2005).

The GLIMPSE I (Benjamin et al. 2003) Catalog (highly reliable), MIPSGAL (Gutermuth & Heyer 2015) catalog, AllWISE (Wright et al. 2010) source catalog and 2MASS (Skrutskie et al. 2006) are used to identify the YSO candidates in this region.

3. Results

3.1. Dust Emission and Clumps

To derive the dust temperature and column density, we fit the spectral energy distribution (SED) with Herschel data. Assuming that the dust emission is optically thin, a graybody radiation model has been used to fit the SED in order to derive the dust temperature T_{D} and the column density N_{H_2} (e.g., Liu et al. 2016)

$$I_{\nu} = k_{\nu_0} \left(\frac{\nu}{\nu_0} \right)^{\beta} B_{\nu}(T_{\text{D}}) \mu m_{\text{H}} N_{\text{H}_2}, \quad (1)$$

where I_{ν} is the surface brightness. The dust opacity is expressed as $k_{\nu} = k_{\nu_0} \left(\frac{\nu}{\nu_0} \right)^{\beta}$, where $k_{\nu_0} = 0.1 \text{ cm}^2 \text{ g}^{-1}$ (Beckwith et al. 1990) and β is the spectral index of the dust opacity which is set to 2.0 (Anderson et al. 2012). $B_{\nu}(T_{\text{D}})$ is the Planck function

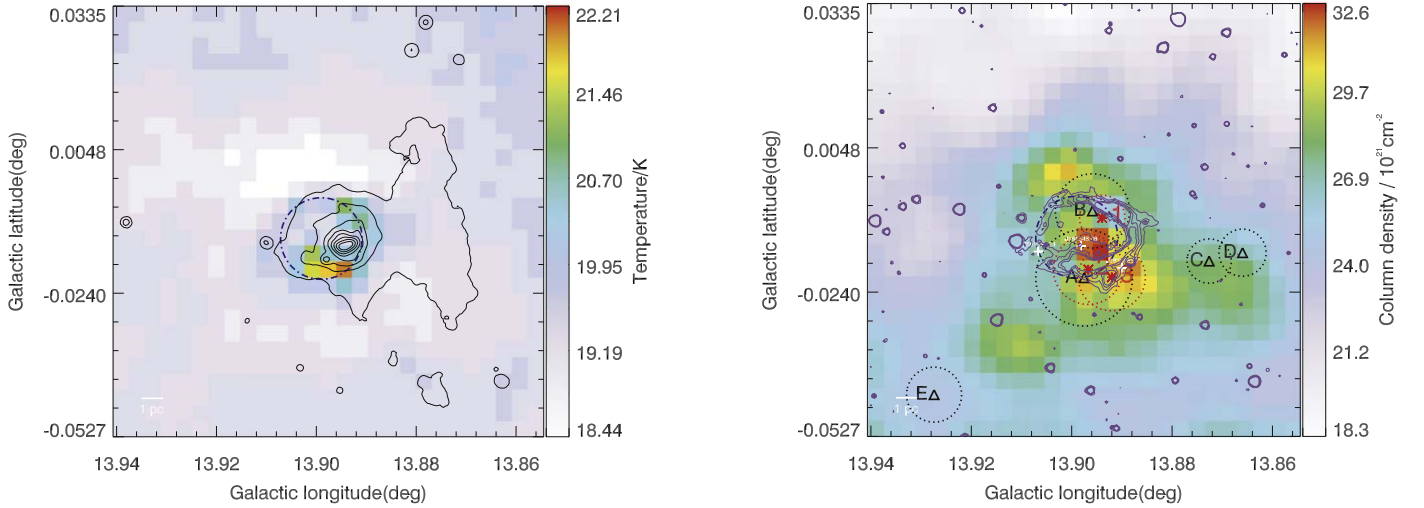


Figure 2. Dust temperature and column density images of N 13. Left panel: The dust temperature image of N 13 overlaid with the contours of the $24\ \mu\text{m}$ emission. The contours start at 10% and go up in steps of 10% of the peak. Right panel: The H_2 column density image overlaid with the contours of $8.0\ \mu\text{m}$ emission with the levels of [120, 130, 140, 150] MJy sr^{-1} . The three red asterisks indicate the dust clumps in Table 1, and the red dashed circle represents the effective radius of dust clumps. The five black triangle symbols indicate the molecular clumps in Table 2, and the black dashed circle represents their effective radius. The three white pluses signify the locations of the YSOs listed in Table 3.

of the dust temperature T_D . The mean molecular weight $\mu = 2.8$ (e.g., Petriella et al. 2010) and m_H is the hydrogen mass. The Herschel 160, 250, 350 and $500\ \mu\text{m}$ data are used for the SED fitting with 20% flux uncertainty (Faimali et al. 2012). The $70\ \mu\text{m}$ data have been excluded since they trace the hotter components with very small grains (VSGs), and warmer material that is heated by protostar(s) and may be optically thick (e.g., Liu et al. 2016).

The derived dust temperature map is shown in the left panel of Figure 2. The dust around the southern edge of N 13 exhibits higher temperatures, suggesting that the H II region inside the bubble N 13 is heating its surroundings. The dust traced by the $24\ \mu\text{m}$ emission can reach very high temperatures after absorbing the Lyman continuum photons (e.g., Deharveng et al. 2010). The temperature distribution is consistent with the $24\ \mu\text{m}$ emission, which is mainly present in the western part of the bubble with a declining radial-gradient out of the shell (see Section 4.1).

The H_2 column density map is displayed in the right panel of Figure 2. The dense parts are mainly located on the layer traced by $8.0\ \mu\text{m}$. Two additional peaks are present to the southwest and east of the bubble. These are far away and may not be associated with bubble N 13 (e.g., Kendrew et al. 2012; Simpson et al. 2012). The mean column density and total mass inside twice the effective radius are $\sim 2.82 \times 10^{22}\ \text{cm}^{-2}$ and $\sim 2.01 \times 10^3\ M_\odot$, respectively.

Elia et al. (2017) derived a band-merged catalog of $\sim 100,000$ dust clumps. Two clumps in the catalog (sources 1 and 2 in Table 1) are spatially matched with the bubble N 13. Elia et al. (2017) adopted a searching radius of $19''$ to cross-match

the APEX Telescope Large Area Survey of the Galaxy (ATLASGAL; Schuller et al. 2009) catalog (Urquhart et al. 2014); the Herschel clumps HIGALBM13.8939-0.0092 and HIGALBM13.8967-0.0195 are excluded from the ATLASGAL catalog (Urquhart et al. 2014). We found the source AGAL013.892-00.021 in the ATLASGAL compact source catalog (CSC; Contreras et al. 2013; Urquhart et al. 2014) is also associated with bubble N 13. The three sources are labeled in the right panel of Figure 2 and summarized in Table 1. All three dust clumps are located at the shell of the bubble. By checking the dust clump catalog derived from the Hi-GAL survey (Elia et al. 2017) and the ATLASGAL survey (Urquhart et al. 2014), we found that two clumps HIGALBM13.8939-0.0092 and HIGALBM13.8967-0.0195 from the former and one source AGAL013.892-0.021 from the latter are located at the shell of N 13. All of them have no counterparts in the other catalog.

3.2. The Molecular Tracers

3.2.1. The Velocity Components

The $^{12}\text{CO}(3-2)$ spectrum of the N 13 region in Figure 3 shows seven CO velocity components. The features with velocities in the ranges -4 – 4 , 108 – 120 , 120 – 128 and 134 – $143\ \text{km s}^{-1}$ are first excluded since they are weak and represent very few detections in the data set. By comparing the integrated intensity images of the components that remained (see Figure 4), the feature with velocities of 22 – $33\ \text{km s}^{-1}$ is likely associated with N 13. We constructed channel maps of this feature with a step size of $1\ \text{km s}^{-1}$ in Figure 5. It can be

Table 1
Dust Clumps Associated with N 13

No.	Designation	EVOL _{FLAG}	SURF _{DENS} (g cm ⁻²)	logN _{H2} (cm ⁻²)	Reference
1	HIGALBM13.8939-0.0092	protostellar	0.064	...	Elia et al. (2017)
2	HIGALBM13.8967-0.0195	protostellar	0.61	...	Elia et al. (2017)
3	AGAL013.892-00.021	YSO	...	21.956	Urquhart et al. (2018)

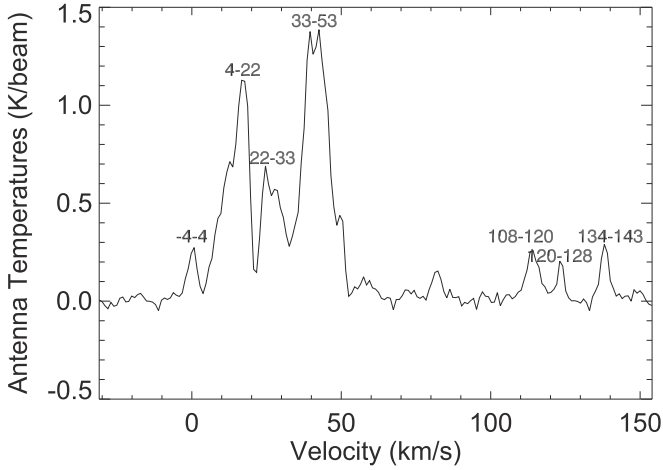


Figure 3. Averaged spectra of the ¹²CO (3-2) emission. Seven components at -4-4, 4-22, 22-33, 33-53, 108-120, 120-128 and 134-143 km s⁻¹ are found.

seen that ¹²CO emission first appears in the southeast part of the map, which is away from N 13. In the range between 23 and 31 km s⁻¹, the CO emission is mainly associated with the bubble, first appearing in the southern part and then in the southern and northern parts. We should note that in the 28–29 km s⁻¹ and 29–30 km s⁻¹ maps, the ¹²CO emission exhibits clear semicircle morphologies. In addition, at velocities of 29–33 km s⁻¹, the ¹²CO emission also appears to the west of N 13, which is approximately 2' from the center of the bubble.

The two-dimensional projection of the emission from the spherical shell of an expanding bubble should exhibit a blueshifted velocity at its front side, a ring-like or arc-like midsection and redshifted velocities at the back cap of the bubble (Beaumont & Williams 2010; Arce et al. 2011). Figure 5 affirms that the ¹²CO emission appears inside the bubble at the velocity of 23–28 km s⁻¹, which may be the front of the bubble N 13 at blueshifted velocities. Then the following components showing semicircle morphologies at 28–30 km s⁻¹ are the arc-like midsection. From the channel maps, the backside of the bubble is not detected with ¹²CO emission. Based on that, the systematic velocity of the bubble, derived by Gaussian fitting, is about 26 km s⁻¹. In summary, the southern, northern and western parts of the bubble appear at 23–26, 25–28 and 28–30 km s⁻¹, respectively. Such a result indicates

that N 13 is not perpendicular to our line of sight, the northern part of the shell is closer to us relative to the system velocity of 26 km s⁻¹, and the southern and western ones are receding from us. This velocity structure of N 13 is consistent with the expanding bubble.

We use the systematic velocity of 26 km s⁻¹ to estimate the kinematic distance (Reid et al. 2019); three possible kinematic distances are derived, i.e., 13.32 ± 0.28 , 12.3 ± 0.28 and 2.95 ± 0.34 kpc with probabilities of 0.33, 0.32 and 0.17, respectively. We then use the H I self-absorption to resolve the distance ambiguity (Anderson & Bania 2009) with the Southern Galactic Plane Survey (SGPS) II H I data (McClure-Griffiths et al. 2005) and find that the kinematic distance of N 13 should be 13.32 ± 0.28 kpc. This distance is consistent with the distances ~ 13.3 , 13.31 and 13.42 kpc of the clumps AGAL013.892–00.021 (Urquhart et al. 2018), HIGALBM13.8939-0.0092 and HIGALBM13.8967-0.0195 (Mège et al. 2021) respectively.

3.2.2. The Molecular Clumps

Molecular clumps in the N 13 region are identified by using the Clumpfind2d algorithm (Williams et al. 1994) with a threshold of $3\sigma_{\text{integral}}$ and increments of $1\sigma_{\text{integral}}$, where $\sigma_{\text{integral}} \approx 3.22$ K km s⁻¹. Five clumps (A-E) are found in the region and are labeled in the right panel of Figure 2. Clumps A and B located on the shell are likely associated with N 13. Clumps C, D and E, far away from the bubble by more than two times the effective radius, have no physical correlation with the bubble N 13 (Kendrew et al. 2012; Simpson et al. 2012). Thus they are not associated with N 13. Furthermore, the ¹²CO emission reveals that the Herschel clumps HIGALBM13.8939-0.0092 and HIGALBM13.8967-0.0195 are associated with Clumps A and B, respectively. In addition, the ATLASGAL source AGAL013.892-00.021 is associated with Clump B.

The column density of the clumps can be roughly estimated as follows (Dickman 1978; Shetty et al. 2011)

$$N_{\text{H}_2} = X \cdot (W_{\text{CO}} \setminus R_{31}) (\text{cm}^{-2}), \quad (2)$$

where $X \sim 6 \times 10^{20}$ cm⁻² K⁻¹ km⁻¹ s (Shetty et al. 2011), W_{CO} is the ¹²CO(3-2) velocity integrated intensity from 22 to 33 km s⁻¹ and $R_{31} = 0.52$ is the CO(3-2)/CO(1-0) luminosity line ratio (Lamperti et al. 2020). The clump mass is then estimated as

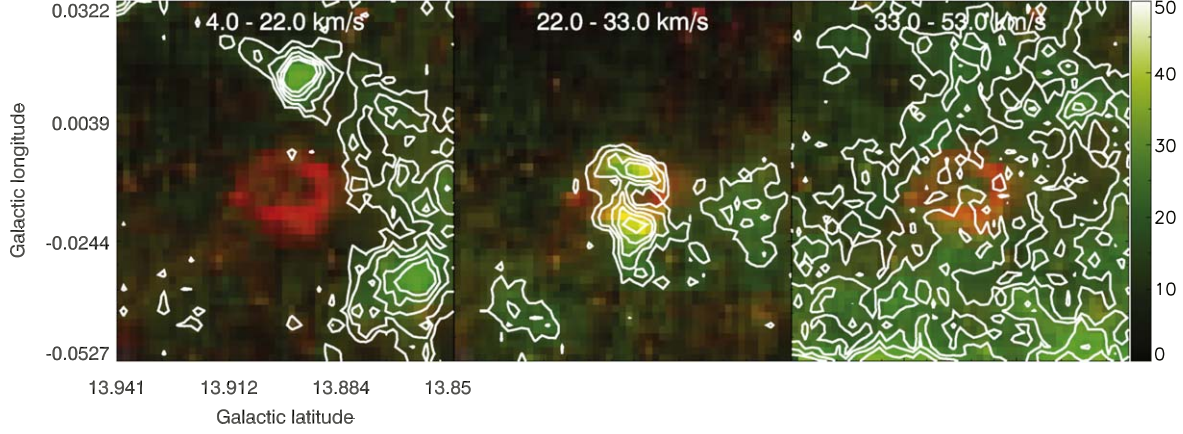


Figure 4. Integrated intensity images of the velocity components of the ^{12}CO (in green) overlaid on the $8.0\ \mu\text{m}$ (in red) emission. The white contours represent the integrated flux of ^{12}CO with the velocity components marked with contour levels at $(3, 4, 5, 6, 7) \times \sigma_{\text{integral}}$, where $\sigma_{\text{integral}} \approx \sqrt{v_2 - v_1} \times \sigma_{\text{rms}}$ and $\sigma_{\text{rms}} = 0.97\ \text{K km s}^{-1}$.

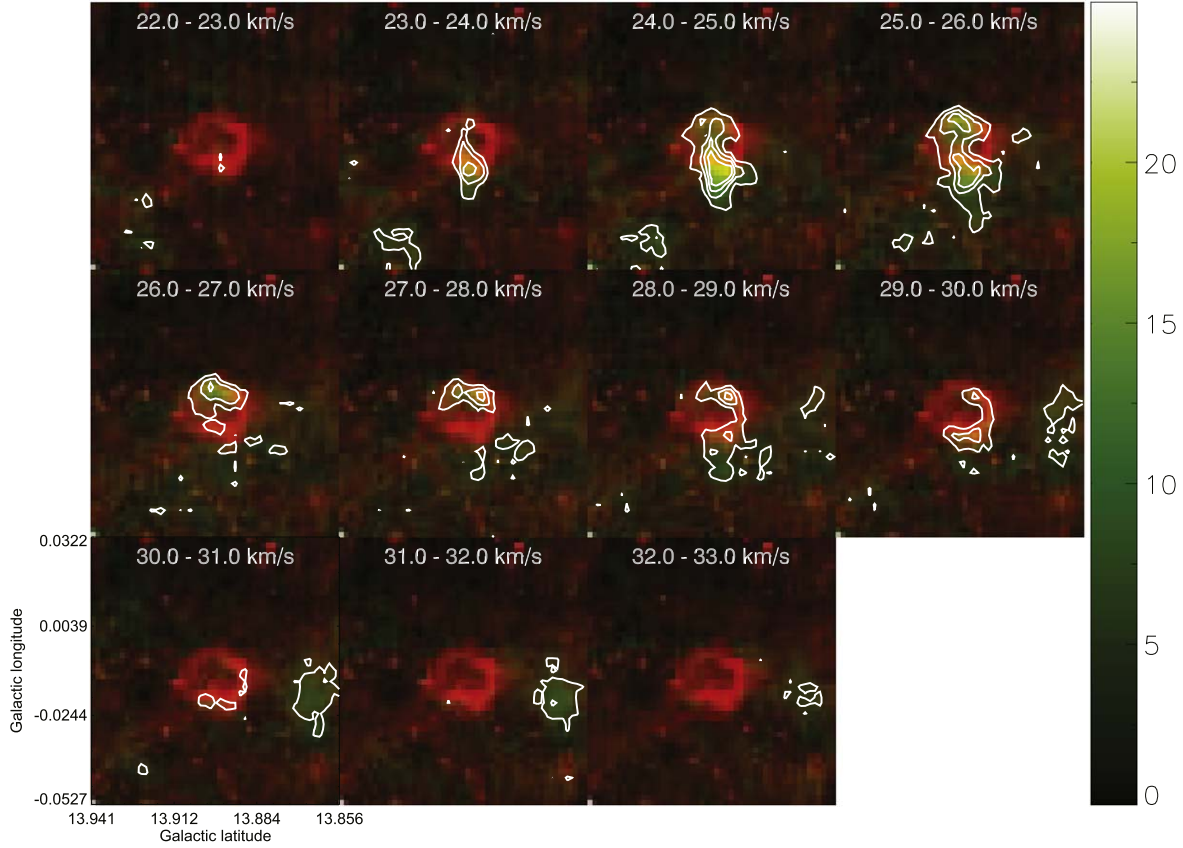


Figure 5. Channel maps of N 13 with a step of $1\ \text{km s}^{-1}$ overlaid on the composite image of the ^{12}CO (in green), $8.0\ \mu\text{m}$ (in red) and $3.6\ \mu\text{m}$ (in blue) emission. The white contours represent the integrated flux of ^{12}CO with the velocity range of $1\ \text{km s}^{-1}$ and with contour levels at $(3, 5, 7, 9, 11) \times \sigma_{\text{rms}}$, where $\sigma_{\text{rms}} = 0.97\ \text{K km s}^{-1}$.

(Buckle et al. 2010)

$$M_{\text{H}_2} = 1.13 \times 10^{-4} \mu_{\text{g}} m_{\text{H}_2} D^2 S N_{\text{H}_2} (M_{\odot}), \quad (3)$$

where the mean atomic weight of the gas $\mu_{\text{g}} = 1.36$, m_{H_2} is the mass of a hydrogen molecule, D is the distance of the clump and S is the clump area in arcsec^2 . Finally, we summarize the

Table 2
Molecular Clump Candidates

Ncl	Npix	Longitude	Latitude	Central Velocity	Velocity Width	Distance	R_{eff}	N_{H_2}	M_{H_2}	M_{vir}	$\frac{M_{\text{clump}}}{M_{\text{vir}}}$	In Shell	Dust Clump No.
		(deg)	(deg)	(km s ⁻¹)	(km s ⁻¹)	(pc)	(pc)	(10 ²² cm ⁻²)	(10 ² M _⊙)	(10 ² M _⊙)			
A	105	13.898	-0.021	25.82	6.93	12.3	2.07	2.75	12.13	51.01	0.24	Y	1
B	62	13.896	-0.008	26.00	5.46	13.32	1.72	2.72	9.77	45.20	0.22	Y	2,3
C	22	13.873	-0.018	28.05	9.30	12.3	0.95	2.15	1.99	21.42	0.09	N	
D	25	13.866	-0.016	28.88	6.66	12.3	1.01	2.19	2.31	1.57	1.47	N	
E	34	13.927	-0.044	26.68	9.87	12.29	1.18	2.03	2.90	0.60	4.84	N	

derived N_{H_2} and M_{H_2} of the clumps in Table 2. Using the same method, the total mass of the entire bubble may be estimated at $\sim 2.19 \times 10^3 M_{\odot}$.

We estimate the virial mass of these molecular clumps by using the ¹³CO (2-1) data of the Structure, Excitation and Dynamics of the Inner Galactic Interstellar Medium (SEDIGISM) survey (Schuller et al. 2021), following the formula (Urquhart et al. 2013)

$$M_{\text{vir}} = \frac{5}{8 \ln 2} \frac{1}{1.3G} R_{\text{eff}} \Delta V_{\text{avg}}^2, \quad (4)$$

where G is the gravitational constant, and R_{eff} is the effective radius of the clump. ΔV_{avg} is the average velocity dispersion of the ¹³CO, and is estimated as (Fuller & Myers 1992)

$$\Delta V_{\text{avg}}^2 = \Delta V_{\text{corr}}^2 + 8 \ln 2 \times \frac{k T_{\text{kin}}}{m_{\text{H}}} \left(\frac{1}{\mu_{\text{p}}} - \frac{1}{\mu_{^{13}\text{CO}}} \right), \quad (5)$$

where ΔV_{corr} is the observed ¹³CO line width for the resolution of the spectrometer (0.25 km s⁻¹ for the SEDIGISM survey), $\Delta V_{\text{corr}}^2 = \Delta V_{\text{obs}}^2 + \Delta V_{\text{channel width}}^2$, k is the Boltzmann constant, T_{kin} is the kinetic temperature, $\mu_{\text{p}} = 2.33$ (Fuller & Myers 1992) is the mean molecular mass of molecular hydrogen and $\mu_{^{13}\text{CO}}$ is the mean molecular mass of ¹³CO (taken as 29.0). Results of the virial mass for clumps and the virial ratios ($M_{\text{clump}}/M_{\text{vir}}$) are listed in Table 2. The virial ratios of Clumps A and B are lower than 1.0 (Urquhart et al. 2013), indicating that Clumps A and B are likely to be unbound.

3.3. The YSO Population

We first identified YSO candidates within the circular region with two times the effective radius of N 13 (0'.98). A total of 214 point sources from the GLIMPSE I and Spring '07 Catalogs (highly reliable) were found. A modified version of the multi-phase source classification scheme (Gutermuth et al. 2009) has been used to further identify YSO candidates of the GLIMPSE catalog with the Spitzer and 2MASS data (see Appendix for details). Eventually, no YSOs are identified. We then sought to identify YSOs following the constraints of Gutermuth et al. (2009) by adding the 2MASS data. Again, no YSOs are found. Then we check the YSO catalog of Spitzer/IRAC (Kuhn et al. 2021). No YSOs are found either.

We also used a classification scheme (Koenig & Leisawitz 2014) by combining the WISE and 2MASS near and mid-infrared emission to search for YSOs in N 13 (see Appendix for details). A total of 31 candidates have been found from the AllWISE catalog within a circular area of 0'.98 radius at the center of N 13. According to the color constraints (Koenig & Leisawitz 2014), all these candidates are excluded. Marton et al. (2016) argued that the classification scheme (Koenig & Leisawitz 2014) is very effective in identifying and removing the Galactic contamination, but allows retrieving a lower number of known YSOs, which may be the reason all the candidates were excluded. We examined the WISE YSO candidate (Marton et al. 2016) and found four YSO candidates (sources 1 to 4 in Table 3) in the N 13 region, three of which are Class I/II YSOs, and the other one is a Class III YSO, which were subsequently detected as evolved stars by using the Gaia Data Release 2 (DR2) catalog (Marton et al. 2019).

We also examined the Gaia DR2 sources (Marton et al. 2019) and found that a YSO with the name 4097493534492719360 (source 5 in Table 3) may be associated with the bubble N 13. However, the distance of the source is 2.24 kpc, which is inconsistent with the distance of 13.32 kpc. This means that source 4097493534492719360 is likely the prospective star.

3.4. Exciting Stars

Figure 1 shows that N 13 is filled with 20 cm free-free radiation. The total fluxes of the 20 cm emission are about 0.25 and 0.32 Jy within an inner radius ($R_{\text{in}} = 0'.57$ and $r_{\text{in}} = 0'.33$) and an outer radius ($R_{\text{out}} = 0'.73$ and $r_{\text{out}} = 0'.42$) of N 13 (Churchwell et al. 2006), respectively. Using these fluxes as lower and upper limits on fluxes of N 13, the number of stellar Lyman photons N_{lyc} can be derived as (Mezger et al. 1974),

$$N_{\text{lyc}} = 4.761 \times 10^{48} \times a(v, T_e)^{-1} \times v^{0.1} \times T_e^{-0.45} \times S_v \times D^2 (\text{ph s}^{-1}), \quad (6)$$

where $a(v, T_e)^{-1}$ is a slowly varying function tabulated by Mezger & Henderson (1967), the electron temperature T_e is assumed to be 10⁴ K, $a(v, T_e) \sim 1$ and S_v is the flux of the 20 cm emission. The number of Lyman photons for N 13 is

Table 3
Magnitudes and Evolution Stages of YSOs

No.	WISE Designation	Gaia DR2 source ID	Longitude (deg)	Latitude (deg)	w1 (mag)	w2 (mag)	w3 (mag)	w4 (mag)	<i>J</i> (mag)	<i>H</i> (mag)	<i>K</i> (mag)	Class	Associated	Reference
1	J181543.98-165247.4	...	13.898	-0.015	11.518 ± 0.059	11.055 ± 0.050	5.867 ± 0.031	1.918 ± 0.029	14.654 ± 0.041	12.918 ± 0.037	12.240 ± 0.033	Class I\II	Y	Marton et al. (2016)
2	J181545.24-165222.2	...	13.907	-0.016	9.055 ± 0.027	8.959 ± 0.025	6.881 ± 0.040	2.811 ± 0.016	13.493 ± 0.035	11.210 ± 0.039	10.184 ± 0.033	Class I\II	Y	Marton et al. (2016)
3	J181543.97-165320.6	...	13.890	-0.019	7.918 ± 0.025	7.825 ± 0.021	6.708 ± 0.033	3.360 ± 0.060	12.882 ± 0.030	10.012 ± 0.026	8.668 ± 0.019	Class I\II	Y	Marton et al. (2016)
4	J181545.84-165231.8	4097493534492881152	13.905	-0.019	9.770 ± 0.029	9.874 ± 0.040	6.639 ± 0.055	3.115 ± 0.023	11.391 ± 0.023	10.425 ± 0.023	10.122 ± 0.026	Class III	N	Marton et al. (2016)
5	J181544.97-165256.3	4097493534492719360	13.898	-0.020	10.312 ± 0.038	10.059 ± 0.038	5.622 ± 0.024	1.992 ± 0.026	11.354 ± 0.023	10.694 ± 0.024	10.508 ± 0.024	YSO	N	Marton et al. (2019)

Table 4
Exciting Star Candidates

No.	R.A. (J2000) (deg)	Decl. (J2000) (deg)	Designation	<i>J</i> (mag)	<i>H</i> (mag)	<i>K</i> (mag)	<i>A_v</i> (mag)	<i>M_J</i> (mag)	<i>M_H</i> (mag)	<i>M_K</i> (mag)	O-type Star	Exciting Star
1	273.93	-16.88	18154371-1652334	15.27	14.43	13.47	12.85	-3.98	-3.44	-3.59	O8-O7	yes
2	273.93	-16.87	18154409-1652293	13.21	12.97	12.63	5.09	-3.86	-3.54	-3.56	O8-O7.5	yes
3	273.93	-16.88	18154260-1652426	15.21	14.27	13.20	14.20	-4.42	-3.84	-4.02	O6.5-O5.5	no
4	273.94	-16.88	18154451-1652300	15.31	13.72	13.09	13.73	-4.19	-4.30	-4.07	O6.5-O6	no
5	273.93	-16.87	18154416-1652263	13.36	13.31	12.59	7.24	-4.31	-3.59	-3.85	O7-O6	yes
6	273.93	-16.87	18154374-1652248	15.37	13.79	13.18	13.55	-4.08	-4.20	-3.97	O7-O6.5	yes
7	273.93	-16.87	18154355-1652209	15.13	14.09	12.99	14.86	-4.69	-4.14	-4.30	O5.5-4	no
8	273.93	-16.88	18154317-1653010	14.34	13.83	12.56	13.74	-5.16	-4.20	-4.60	O5-O3	no
9	273.93	-16.87	18154323-1652205	15.04	13.90	13.42	10.48	-3.54	-3.57	-3.38	O9-O8.5	no
10	273.93	-16.88	18154216-1652366	15.70	14.39	13.20	16.84	-4.68	-4.19	-4.31	O5.5-O4	no
11	273.93	-16.87	18154263-1652224	14.93	12.89	12.78	11.72	-4.00	-4.79	-4.16	O7.5-O5.5	no
12	273.93	-16.87	18154229-1652267	14.67	13.71	12.96	11.76	-4.27	-3.97	-3.99	O6.5-O6	no
13	273.93	-16.87	18154346-1652161	14.28	13.13	12.97	7.98	-3.60	-3.89	-3.55	O9-O8	no
14	273.93	-16.87	18154236-1652243	14.54	13.45	12.83	11.33	-4.28	-4.16	-4.06	O6.5-O6	no
15	273.92	-16.87	18154184-1652298	15.48	13.68	13.17	13.78	-4.03	-4.36	-4.00	O7.5-O6	no
16	273.93	-16.87	18154313-1652131	15.51	14.31	13.15	16.11	-4.66	-4.13	-4.28	O5.5-O4	no

then $N_{\text{lyc}} = (3.53 - 4.51) \times 10^{48} \text{ ph s}^{-1}$. This result indicates the presence of a massive O7.5V–O7V star or a group of smaller stars in order to account for the derived Lyman photons (Martins et al. 2005).

Then we search for the exciting star(s) among all IR point sources inside bubble N 13 within the GLIMPSE I Spring '07 Point Source Catalog and 2MASS Point Source Catalog. Any candidate sources cannot be identified as YSOs and they should have effective detections in all three 2MASS bands. Based on these criteria, 11 and 45 point sources are found from the GLIMPSE and 2MASS catalogs, respectively. Adopting a distance of $13.34 \pm 0.28 \text{ kpc}$ (Section 3.2.1) and using a near-infrared extinction law of Rieke & Lebofsky (1985) ($A_J/A_V = 0.282$ with $A_H/A_V = 0.175$ and $A_{K_s}/A_V = 0.112$), and the intrinsic color $[J - H]_0$ and $[H - K_s]_0$ obtained from Martins & Plez (2006), we derive the interstellar extinction and calculate the J, H and Ks absolute magnitudes of these candidate sources. Eventually, 16 candidate O-type stars are found to be associated with N 13 and they are listed in Table 4 and labeled in Figure 6. As mentioned before, the exciting star(s) should be at least between O7.5 and O7V or be a group of smaller ones. Sources 1, 2, 5, 6, 9, 11, 13 and 15 could be the exciting star candidates. Then according to the standard procedure described in Pomarès et al. (2009), the exciting star(s) are expected to be near the center of the H II region, which makes sources 1, 2, 5 and 6 the most likely exciting stars of N 13.

4. Discussion

4.1. The Morphology of N 13

As demonstrated in Figure 1, the $8 \mu\text{m}$ emission traces the bright shell of N 13, meanwhile, the cavity is filled with $24 \mu\text{m}$ and 20 cm emissions. A color image of the $24 \mu\text{m}$ emission is

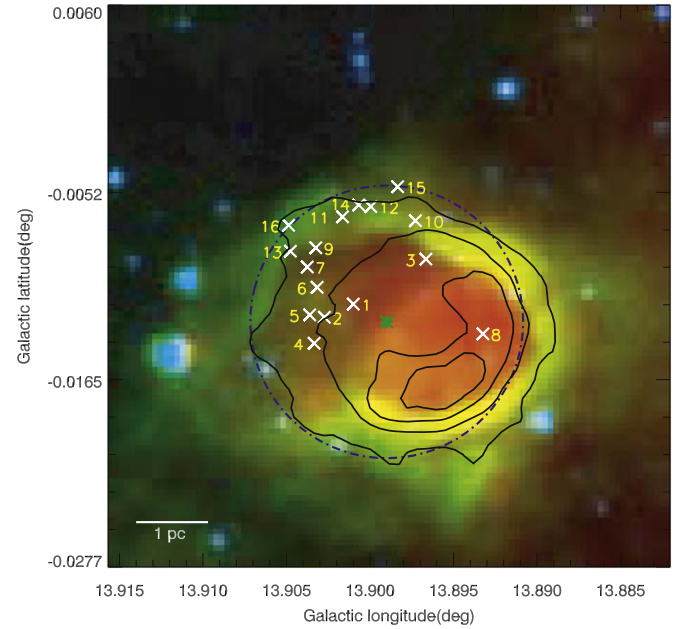


Figure 6. Distributions of exciting stars (white crosses) on the composite three color image with 3.6 (blue), 8.0 (green) and $24 \mu\text{m}$ (red) emissions. The black contours represent the MAGPIS 20 cm emission. The green asterisk and blue dashed circle indicate the center and effective radius of N 13, respectively.

given in the left panel of Figure 7. The map confirms that the $24 \mu\text{m}$ emission is mainly located in the bubble and exceeds the shell in the west showing a sector morphology and gradually decreasing intensities toward the west. We can see in Figure 2 that relatively high temperatures are also presented beyond the shell in the west part. In contrast, smaller column densities are present there. In addition, there is also a distinct CO component

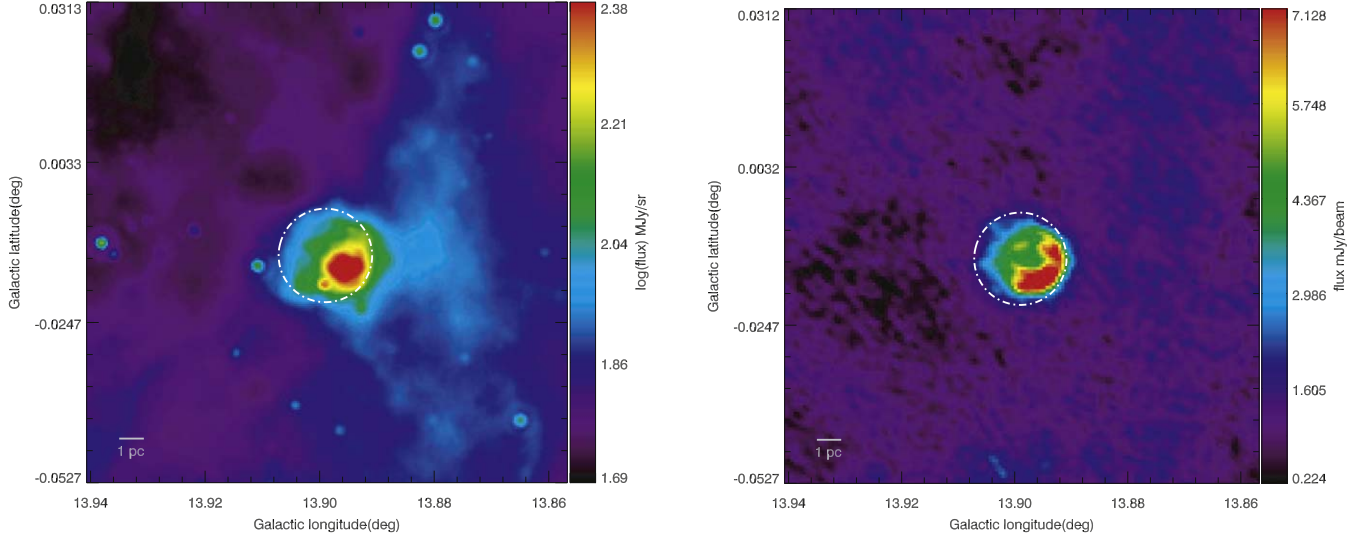


Figure 7. Color images of the $24\ \mu\text{m}$ emission (left) and the $20\ \text{cm}$ emission (right) of N 13. The σ_{rms} values are $\sim 0.6\ \text{MJy sr}^{-1}$ and $\sim 0.00065\ \text{Jy beam}^{-1}$ for the $24\ \mu\text{m}$ and $20\ \text{cm}$, respectively. The white dashed circle represents the effective radius of N 13.

to the west of N 13 (see, e.g., the $29\text{--}30\ \text{km s}^{-1}$ map in Figure 5). All the results suggest that the bubble might be erupting toward the west.

The $20\ \text{cm}$ emission mainly concentrates in the cavity with spillover in the western region, which is similar to the central part of the $24\ \mu\text{m}$ emission (see the right panel of Figure 7). It indicates that the ionizing radiation and the warm dust are systematically correlated (Deharveng et al. 2010; Paladini et al. 2012). Furthermore, as shown in Figure 7, the $24\ \mu\text{m}$ and $20\ \text{cm}$ emissions are mainly confined within the cavity of N 13. This also indicates that the shell of N 13 has not been destroyed and the bubble is likely in an early evolutionary stage.

From the right panel of Figure 2 and the integrated intensity images of ^{12}CO (the middle panel of Figure 4), the densest region is present on the layer traced by $8.0\ \mu\text{m}$. At the same time, molecular gas appears toward the southeast and the west at more than two times the radius of the bubble N 13. These molecular components may not be associated with bubble N 13. Another possible explanation is that these regions are less dense and are more easily accelerated by the exciting star(s).

4.2. Star Formation in the Clumps

As mentioned in Section 3.1 and 3.2, three dust clumps and two molecular clumps are found in N 13, and they are indicated by the red asterisks and black triangle symbols in the right panel of Figure 2, respectively.

First, the Herschel sources HIGALBM13.8939-0.0092 and HIGALBM13.8967-0.0195 with surface densities of 0.064 and $0.61\ \text{g cm}^{-2}$ (see Table 1) are between 0.05 and $1\ \text{g cm}^{-2}$ (Urquhart et al. 2013), which means that the two targets can form massive stars. The ATLASGAL source AGAL013.892-

00.021 is identified as pre-stellar cores with a column density exceeding $N_{\text{H}_2} = 7 \times 10^{21}\ \text{cm}^{-2}$ (André et al. 2011), and they indicate that it may be capable of forming stars. In addition, the mass of ATLASGAL clump AGAL013.892-00.021 of $\sim 2594 M_{\odot}$ given by Urquhart et al. (2018) is heavier than $m(r) = 870 M_{\odot} \left(\frac{r}{\text{pc}}\right)^{1.33}$ (Kauffmann et al. 2010), which implies the possibility of massive star formation in clump AGAL013.892-00.021.

Three YSOs listed in Table 3 have been identified in N 13 (see Section 3.3), which are indicated by the white plus symbols in the right panel of Figure 2. Candidates 2 and 3 are on the shell layer of the bubble, and candidate 1 is near the bubble center. Candidates 1 and 3 are located in dense regions, implying that those two YSOs may be associated with the bubble N 13. However, we cannot find evidence for the triggered star formation of the bubble by using the distributions of the few YSOs.

4.3. Triggered Star Formation

Assuming the H II region expands in a homogeneous molecular cloud, the dynamical age of N 13 can be estimated using the expression (Dyson & Williams 1980)

$$t(R) = \frac{4 R_s}{7 C_s} \left[\left(\frac{R}{R_s} \right)^{\frac{7}{4}} - 1 \right], \quad (7)$$

where $R = 0.49$ is the radius of the bubble, $C_s = 10^6\ \text{cm s}^{-1}$ is the sound velocity in the ionized gas, R_s is the radius of the Strömgen sphere given by $R_s = (3N_{\text{lyc}}/4\pi n_0^2 \alpha_B)^{\frac{1}{3}}$, $\alpha_B = 2.6 \times 10^{-13}\ \text{cm}^3\ \text{s}^{-1}$ is the hydrogen recombination

Table 5
Physical Parameters of the 10 Bubbles

No.	IR Bubble	Longitude (deg)	Latitude (deg)	Radius of bubble (pc)	Number of dust clumps	Number of molecular clumps	Number of YSOs	Lyman Photons ($10^{48} \text{ ph s}^{-1}$)	Dynamical Age (Myr)	Fragmentation Time (Myr)	Mod.	Reference
1	N 10	13.188	0.039	1.6 ^a	...	2 ^b	15	22	0.0917 ^a	1.5 ^b	RDI ^b	Watson et al. (2008)
2	N 22	18.254	-0.305	1.77	...	11	24	42 ~ 94	0.06 ~ 0.15	1.36 ~ 2.93	RDI	Ji et al. (2012)
3	N 13	13.900	-0.014	1.9	3	2	3	3.35 ~ 4.51	0.32 ~ 0.35	1.37~2.80	RDI	This paper
4	N 4	11.892	0.748	1.9	6	...	60	0.4 ~ 2.6	~1.0	~0.3	C&C	Liu et al. (2016)
5	N 49	28.827	-0.229	1.95	...	17	52	~2.0	0.83	0.9	C&C	Dirienzo et al. (2012)
6	N 92	44.333	-0.839	2.59	...	13	35	~0.2	2.12	1.7	C&C	Dirienzo et al. (2012)
7	G24.136 +00.436	24.136	0.436	3.9	...	6	63	1.11 ~ 1.19	1.5 ~ 1.6	1.5 ~ 1.7	C&C	Liu et al. (2015)
8	N 91	44.211	0.05	6.4	...	45	178	~2.0	2.41	1.7	C&C	Dirienzo et al. (2012)
9	N 24	18.908	-0.315	15.0	23	...	11	73.4	1.5 ~ 4.0	2.70 ~ 5.44	C&C/RDI	Li et al. (2019)
10	G015684- 002904	15.684	-0.29	15.7	39	19	49	2.6 ~ 5.2	2.55 ~ 3.42	0.82 ~ 1.74	C&C	Zhou et al. (2020)

Notes.^a Ma et al. (2013).^b Gama et al. (2016).

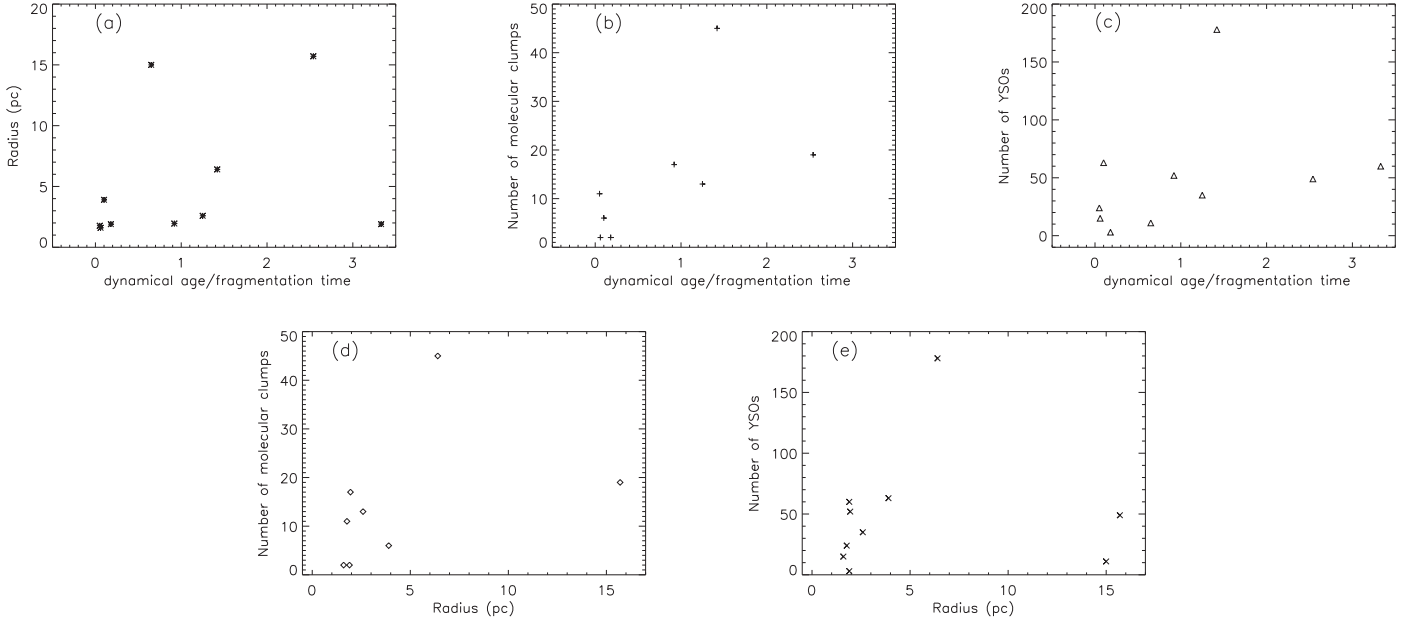


Figure 8. (a)–(c) The effective radius of the bubble, molecular clumps and YSOs vs. the ratio of kinetic age against the fragmentation time. (d), (e) Molecular clumps and YSOs vs. the line scale.

coefficient to all levels above the ground level and $n_0 \sim 1.57 \times 10^3 \text{ cm}^{-3}$ is the original ambient density by assuming the bubble structure is a sphere and the distance is $13.34 \pm 0.28 \text{ kpc}$. This suggests that the dynamical age of N 13 is 0.32–0.35 Myr.

The fragmentation time is the time that an expanding H II region sweeps and collects gas materials around it, forms a shell and then fragments into clumps. It can be estimated by the theoretical models in Whitworth et al. (1994)

$$t_{\text{fragment}} = 1.56 \left(\frac{\alpha_s}{0.2} \right)^{\frac{7}{11}} \left(\frac{N_{\text{lyc}}}{10^{49}} \right)^{-\frac{1}{11}} \left(\frac{n_0}{10^3} \right)^{-\frac{5}{11}}, \quad (8)$$

where $\alpha_s = 0.2\text{--}0.6 \text{ km s}^{-1}$ is the turbulent velocity in the collected layer (Whitworth et al. 1994). The fragmentation time of the collected layer of N 13 would be 1.37–2.80 Myr.

The dynamical age of N 13 is significantly less than the fragmentation time of the collected layer, which implies that fragmentation of the collected layer may not have occurred in the period from the formation of the bubble to the present. In other words, if the second-generation young stars form at this evolution stage, then they are more likely triggered by the RDI mechanism rather than the C&C mechanism.

4.4. A Brief Comparison with Bubbles in Literature

Past studies suggest that large-size bubbles may have more time to sweep and collect the surrounding materials, and so more chance to trigger active star formation, such as N 6 (Yuan et al. 2014) and G15.684-0.29 (Zhou et al. 2020). In Zhou et al.

(2020), we performed a multi-wavelength study on one of the largest bubbles G15.684-0.29 (with a radius of 15.7 pc) and have identified 39 dense cold clumps, 19 molecular clumps, 9 Class I YSOs, 28 Class II YSOs and 12 transition disks around the bubble. Furthermore, we found that the dynamical age of $\sim 4 \text{ Myr}$ is much greater than the shell fragmentation time of 0.82–1.74 Myr for bubble G15.684–0.29, which suggests that the C&C model may be dominant there. We compared the large-size bubble G15.684–0.29 with N 13 and found that the large one has more dust clumps, molecular clumps and YSOs than the small-size bubble. The dynamic age of the large-size bubble is greater than that of the small one, but the fragmentation times of the two bubbles are relatively similar. The primary mechanism for triggering the star formation of two bubbles may thus be different.

The comparisons of the two bubbles show that star formation activity is more active in the large-size bubble G15.684–0.29. Furthermore, we make a brief comparative study of ten bubbles found in literature (see Table 5 and Figure 8). Figures 8(a)–(c) display the comparisons of the effective radius, molecular clumps and YSOs vs. the ratio of kinetic age against the fragmentation time of the sample, respectively. These results suggest that the effective radii of the bubble, molecular clumps and YSOs increase within the increasing ratio. Figures 8(d) and (e) show the numbers of molecular clumps and YSOs against the effective radius of the bubbles. There are no distinct trends of the number of molecular clumps and YSOs from the small-size bubbles to the large-size ones. However, we find that triggering star formation is more active in the bubbles with a

larger ratio of kinetic to fragmentation time, and the C&C mechanism may play the dominant role in the large-size ones.

As described above, the triggered star formation seems to be more active in bubbles with larger ratio of kinetic age against the fragmentation time. The C&C model may play more important roles in the large-size bubbles, while the RDI model may work in the small-size ones. This is consistent with previous studies (e.g., Petriella et al. 2010; Ji et al. 2012), where the C&C and RDI models also play a dominant role in different cases. It is worth noting that our brief comparative work on bubbles is a small sample and that the study criteria for these samples are not uniform. It is significant to conduct a systematic study with a larger sample of different sizes to achieve a comprehensive understanding of the feedback from the bubble and to verify whether the C&C and RDI models may dominate at different sizes or evolutionary stages. Therefore, we have selected 226 isolated bubbles of different sizes, and plan to study some of them in a future paper.

5. Summary

Our main conclusions are summarized as follows.

1. There are three dust clumps identified from the Hi-GAL and ATLASGAL surveys around the bubble N 13, and they all may form massive stars. We also identified five molecular cores with the JCMT $^{12}\text{CO}(3-2)$ data, and two clumps, A and B, lie in the shell of bubble N 13 and may be capable of forming stars.
2. Three Class I/II YSOs have been found within a radius of $0'.98$ around N 13. We have identified four O-type stars inside the bubble N 13, and these may be exciting stars. The fragmentation age of the bubble is 1.37–2.80 Myr, which is greater than the dynamical age of 0.32–0.35 Myr. The RDI model may play a more important role in triggering star formation.
3. Discrepancies are found between bubble N 13 ($R \sim 1.9$ pc) and G15.684–0.29 ($R \sim 15.7$ pc). The numbers of dust clumps, molecular clumps and YSOs of bubble N 13 are less than for bubble G15.684–0.29, and the dynamic age is smaller. Moreover, they may have different mechanisms for triggering star formation.
4. Comparisons of 10 bubbles show that bubbles with larger ratio of kinetic age against the fragmentation time seem to have larger sizes, more clumps and YSOs, which imply that star formation is more active in the bubbles with a larger ratio of kinetic age against fragmentation time. In addition, we also found that the C&C mechanism may play the dominant role in the large-size ones.

Acknowledgments

This work was funded by the CAS “Light of West China” Program under Grant No. 2021-XBQNXZ-028, the National

Key R&D Program of China No. 2022YFA1603103, and the National Natural Science Foundation of China (NSFC, Grant Nos. 12103082, 11973076, 11903070 and 12173075), partially funded by the CAS “Light of West China” Program under Grant No. 2020-XBQNXZ-017, the CAS Presidents International Fellowship Initiative with Grant No. 2022VMA0019, the Natural Science Foundation of Xinjiang Uygur Autonomous Region under Grant No. 2022D01E06, and the Project of Xinjiang Uygur Autonomous Region of China for Flexibly Fetching in Upscale Talents. G.W. acknowledges the support from Youth Innovation Promotion Association CAS.

Appendix Identification of YSOs

In our work, we used the multi-phase source classification scheme presented by Gutermuth et al. (2009) to identify YSOs of the GLIMPSE catalog with the Spitzer and 2MASS data. First, we pick out 16 sources from those 214 sources, following the photometric detections in all four IRAC bands ($\sigma < 0.2$ mag). Second, we remove one polycyclic aromatic hydrocarbon (PAH)-contaminated source from those 16 sources following constraints (Gutermuth et al. 2009): $[3.6]-[4.5]-\sigma_2 \leq 1.4 \times (([4.5]-[5.8]) + \sigma_1 - 0.7) + 0.15$ and $[3.6]-[4.5]-\sigma_2 < 1.65$, where $\sigma_1 = \sigma\{[4.5]-[5.8]\}$ and $\sigma_2 = \sigma\{[3.6]-[4.5]\}$. Third, we identify Class I and II YSOs following the constraints: $[4.5]-[5.8] > 0.7$ and $[3.6]-[4.5] > 0.7$, and the constraints: $[4.5]-[8.0] - \sigma_3 > 0.5$, $[3.6]-[5.8] - \sigma_4 > 0.35$, $[3.6]-[5.8] + \sigma_4 \leq 3.5 \times (([4.5]-[8.0]-\sigma_3) - 0.5) + 0.5$ and $[3.6]-[4.5] - \sigma_2 > 0.15$, where $\sigma_3 = \sigma\{[4.5]-[8.0]\}$ and $\sigma_4 = \sigma\{[3.6]-[5.8]\}$.

We used the classification scheme presented by Koenig & Leisawitz (2014) to identify YSOs of the AllWISE catalog. A total of 31 candidates are found in the AllWISE catalog within a circular area for $0'.98$ radii at the center of N 13. First, with a non-null photometric error in WISE bands 1, 2 and 3, Class I YSO should meet the constraints: $w_2 - w_3 > 2.0$, $w_1 - w_2 > -0.42 \times (w_2 - w_3) + 2.2$, $w_1 - w_2 > 0.46 \times (w_2 - w_3) - 0.9$ and $w_2 - w_3 < 4.5$. Class II YSO should meet the constraints: $w_1 - w_2 > 0.25$, $w_1 - w_2 < 0.9 \times (w_2 - w_3) - 0.25$, $w_1 - w_2 > -1.5 \times (w_2 - w_3) + 2.1$, $w_1 - w_2 > 0.46 \times (w_2 - w_3) - 0.9$ and $w_2 - w_3 < 4.5$, where w_1 , w_2 and w_3 are the instrumental profile-fit photometry magnitude of WISE bands 1, 2 and 3. We also search for YSOs with non-null photometric error in 2MASS H and Ks bands, and the WISE band 1 requirements non-null $w1sigmpro$ and $w1rchi2 < (w1snr - 3)/7$, and the WISE band 2 requirements non-null $w2sigmpro$. The YSOs using the criteria: $H - Ks > 0.0$, $H - Ks > -1.76 \times (w_1 - w_2) + 0.9$, $H - Ks < (0.55/0.16) \times (w_1 - w_2) - 0.85$ and $w_1 \leq 13.0$, where $w1sigmpro$ and $w2sigmpro$ are the instrumental profile-fit photometry flux uncertainty in mag units of WISE bands 1 and 2, and $w1rchi2$ and $w1snr$ are the instrumental profile-fit photometry reduced χ^2 and the signal-to-noise ratio of band 1,

respectively. H and K_s are the H and K_s magnitudes respectively.

References

- Anderson, L. D., & Bania, T. M. 2009, *ApJ*, 690, 706
- Anderson, L. D., Bania, T. M., Balsler, D. S., et al. 2014, *ApJS*, 212, 1
- Anderson, L. D., Zavagno, A., Barlow, M. J., et al. 2012, *A&A*, 537, A1
- André, P., Men'shchikov, A., Könyves, V., et al. 2011, in *Computational Star Formation*, Vol. 255
- Arce, H. G., Borkin, M. A., Goodman, A. A., et al. 2011, *ApJ*, 742, 105
- Beaumont, C. N., & Williams, J. P. 2010, *ApJ*, 709, 791
- Beckwith, S. V. W., Sargent, A. I., Chini, R. S., et al. 1990, *AJ*, 99, 924
- Benjamin, R. A., Churchwell, E., Babler, B. L., et al. 2003, *PASP*, 115, 953
- Bertoldi, F. 1989, *ApJ*, 346, 735
- Buckle, J. V., Curtis, E. I., Roberts, J. F., et al. 2010, *MNRAS*, 401, 204
- Carey, S. J., Noriega-Crespo, A., Mizuno, D. R., et al. 2009, *PASP*, 121, 76
- Churchwell, E. 2002, *ARA&A*, 40, 27
- Churchwell, E., Povich, M. S., Allen, D., et al. 2006, *ApJ*, 649, 759
- Churchwell, E., Watson, D. F., Povich, M. S., et al. 2007, *ApJ*, 670, 428
- Contreras, Y., Schuller, F., Urquhart, J. S., et al. 2013, *A&A*, 549, A45
- Deharveng, L., Schuller, F., Anderson, L. D., et al. 2010, *A&A*, 523, A6
- Dempsey, J. T., Thomas, H. S., & Currie, M. J. 2013, *ApJS*, 209, 8
- Dickman, R. L. 1978, *ApJS*, 37, 407
- Dirienzo, W. J., Indebetouw, R., Brogan, C., et al. 2012, *AJ*, 144, 173
- Dyson, J. E., & Williams, D. A. 1980, *Natur*, 287, 373
- Elia, D., Molinari, S., Schisano, E., et al. 2017, *MNRAS*, 471, 100
- Elmegreen, B. G., & Lada, C. J. 1977, *ApJ*, 214, 725
- Faimali, A., Thompson, M. A., Hindson, L., et al. 2012, *MNRAS*, 426, 402
- Fuller, G. A., & Myers, P. C. 1992, *ApJ*, 384, 523
- Gama, D. R. G., Lepine, J. R. D., Mendoza, E., et al. 2016, *ApJ*, 830, 57
- Griffin, M. J., Abergel, A., Abreu, A., et al. 2010, *A&A*, 518, L3
- Gutermuth, R. A., & Heyer, M. 2015, *AJ*, 149, 64
- Gutermuth, R. A., Megeath, S. T., Myers, P. C., et al. 2009, *ApJS*, 184, 18
- Ji, W.-G., Zhou, J.-J., Esimbek, J., et al. 2012, *A&A*, 544, A39
- Kauffmann, J., Pillai, T., Shetty, R., et al. 2010, *ApJ*, 716, 433
- Kendrew, S., Simpson, R., Bressert, E., et al. 2012, *ApJ*, 755, 71
- Koenig, X. P., & Leisawitz, D. T. 2014, *ApJ*, 791, 131
- Kuhn, M. A., de Souza, R. S., Krone-Martins, A., et al. 2021, *ApJS*, 254, 33
- Lamperti, I., Saintonge, A., Koss, M., et al. 2020, *ApJ*, 889, 103
- Lefloch, B., & Lazareff, B. 1994, *A&A*, 289, 559
- Li, X., Esimbek, J., Zhou, J., et al. 2019, *MNRAS*, 487, 1517
- Liu, H.-L., Li, J.-Z., Wu, Y., et al. 2016, *ApJ*, 818, 95
- Liu, H.-L., Wu, Y., Li, J., et al. 2015, *ApJ*, 798, 30
- Ma, Y., Zhou, J., Esimbek, J., et al. 2013, *Ap&SS*, 345, 297
- Martins, F., & Plez, B. 2006, *A&A*, 457, 637
- Martins, F., Schaerer, D., & Hillier, D. J. 2005, *A&A*, 436, 1049
- Marton, G., Ábrahám, P., Szegedi-Elek, E., et al. 2019, *MNRAS*, 487, 2522
- Marton, G., Tóth, L. V., Paladini, R., et al. 2016, *MNRAS*, 458, 3479
- McClure-Griffiths, N. M., Dickey, J. M., Gaensler, B. M., et al. 2005, *ApJS*, 158, 178
- Mège, P., Russeil, D., Zavagno, A., et al. 2021, *A&A*, 646, A74
- Mezger, P. G., & Henderson, A. P. 1967, *ApJ*, 147, 471
- Mezger, P. G., Smith, L. F., & Churchwell, E. 1974, *A&A*, 32, 269
- Molinari, S., Swinyard, B., Bally, J., et al. 2010, *A&A*, 518, L100
- Paladini, R., Umama, G., Veneziani, M., et al. 2012, *ApJ*, 760, 149
- Petriella, A., Paron, S., & Giacani, E. 2010, *A&A*, 513, A44
- Pogltisch, A., Waelkens, C., Geis, N., et al. 2010, *A&A*, 518, L2
- Pomarès, M., Zavagno, A., Deharveng, L., et al. 2009, *A&A*, 494, 987
- Reid, M. J., Pesce, D. W., & Riess, A. G. 2019, *ApJL*, 886, L27
- Rieke, G. H., & Lebofsky, M. J. 1985, *ApJ*, 288, 618
- Schuller, F., Menten, K. M., Contreras, Y., et al. 2009, *A&A*, 504, 415
- Schuller, F., Urquhart, J. S., Csengeri, T., et al. 2021, *MNRAS*, 500, 3064
- Shetty, R., Glover, S. C., Dullemond, C. P., et al. 2011, *MNRAS*, 412, 1686
- Simpson, R. J., Povich, M. S., Kendrew, S., et al. 2012, *MNRAS*, 424, 2442
- Skrutskie, M. F., Cutri, R. M., Stiening, R., et al. 2006, *AJ*, 131, 1163
- Thompson, M. A., Urquhart, J. S., Moore, T. J. T., et al. 2012, *MNRAS*, 421, 408
- Urquhart, J. S., Csengeri, T., Wyrowski, F., et al. 2014, *A&A*, 568, A41
- Urquhart, J. S., König, C., Giannetti, A., et al. 2018, *MNRAS*, 473, 1059
- Urquhart, J. S., Moore, T. J. T., Schuller, F., et al. 2013, *MNRAS*, 431, 1752
- Urquhart, J. S., Thompson, M. A., Moore, T. J. T., et al. 2013, *MNRAS*, 435, 400
- Watson, C., Povich, M. S., Churchwell, E. B., et al. 2008, *ApJ*, 681, 1341
- Weaver, W. B., & Torres-Dodgen, A. V. 1997, *ApJ*, 487, 847
- White, R. L., Becker, R. H., & Helfand, D. J. 2005, *AJ*, 130, 586
- Whitworth, A. P., Bhattal, A. S., Chapman, S. J., et al. 1994, *MNRAS*, 268, 291
- Williams, J. P., de Geus, E. J., & Blitz, L. 1994, *ApJ*, 428, 693
- Wright, E. L., Eisenhardt, P. R. M., Mainzer, A. K., et al. 2010, *AJ*, 140, 1868
- Yuan, J.-H., Wu, Y., Li, J. Z., et al. 2014, *ApJ*, 797, 40
- Zhang, C.-P., & Wang, J.-J. 2013, *RAA*, 13, 47
- Zhou, J., Zhou, D., Esimbek, J., et al. 2020, *ApJ*, 897, 74